



Shedding Light on the Effect of Diethyl Ether Antisolvent on the Growth of $(\text{CH}_3\text{NH}_3)\text{PbI}_3$ Thin Films

AMAL BOUICH,^{1,2,5} BERNABÉ MARI,¹ LAHOUCINE ATOURKI,^{3,4}
SHAFI ULLAH,¹ and MOHAMED EBN TOUHAMI²

1.—Institute de Disseny i Fabricació, Universitat Politècnica, Valencia, Spain. 2.—Laboratoire (LMEE), Ibn Tofail University of Kenitra, Kenitra, Morocco. 3.—MANAPSE, Faculty of Sciences, Mohammed V University in Rabat, Rabat, Morocco. 4.—Materials and Renewable Energies Laboratory, Ibn Zohar University, Agadir, Morocco. 5.—e-mail: bouich.amal@gmail.com

Antisolvent behavior is one of the most important treatments for producing high-quality perovskite MAPbI_3 thin films. However, the optimization of the amount of antisolvent used has not been analyzed on a uniform platform. In this work, a systematic study is employed to quantitatively evaluate the impact of anti-solvent treatment on the morphological, structural, and optoelectronic characteristics of MAPbI_3 films. The results confirm that an adequate amount of 2.5 ml with a slow annealing treatment leads to homogeneous perovskite films with virtually no holes and large grain size. Using antisolvent treatment and optimized thermal annealing, we were able to control the nucleation and growth of the MAPbI_3 , and therefore achieve highly compact perovskite films with large grains, excellent crystalline quality, and very low pinhole density. The results of this study could help establish reproducible manufacturing processes for perovskite solar cells.

INTRODUCTION

Perovskite has good optical and electronic properties that make it among the best semiconductors, with good absorption throughout the visible spectrum interval, a direct bandgap from 1.5 eV to 2.3 eV,^{1,2} and the capacity to transfer electrons and holes.³ To produce perovskite films with high quality, a variety of methods have been used, including solution processes via spin-coating of precursors, and among the most used processes single-step solution deposition is frequently used because of the simplicity of manufacture and low manufacturing costs.^{4,5} Two-step solution deposition which it is easy to control is widely used for the elaboration of thin layers of perovskites,⁶ two-step vapor-assisted deposition, this process permits good control of thin-film surface, particle grain size,⁷ and thermal vapor deposition generally used for making good layers with regular thickness.⁸ In our case, we used the one-step deposition by spin-coating. This technique demonstrates the capacity for a wide scale of perovskite solar cell manufacture and a higher efficiency

of devices than the other techniques, in particular, spin-coated devices associated with controlling the surface morphology and further the structure formation. It has been documented that the surface morphology is one of the most important parameters that affect the performance of perovskite solar cells. To improve the surface homogeneity and to modulate the perovskite crystal's growth, many methods and treatments have been introduced.

Crystallization is accomplished by slowing down the solubility in a saturated solution by evaporation, cooling, adding antisolvent, or mixing the above procedures. In our work, the film surface was treated by adding diethyl ether (ET) antisolvent with different rates that directly influence the level of supersaturation and thermal annealing. During the treatment, complex exchanges appear at the same time under the influence of several physico-chemical properties. A whole understanding of this topic is critically important for improving solar cell performance.

In this work, we studied the effect of different amounts of ET on tailoring the properties of MAPbI_3 films. The obtained perovskite thin films were studied by scanning electron microscopy (SEM), x-

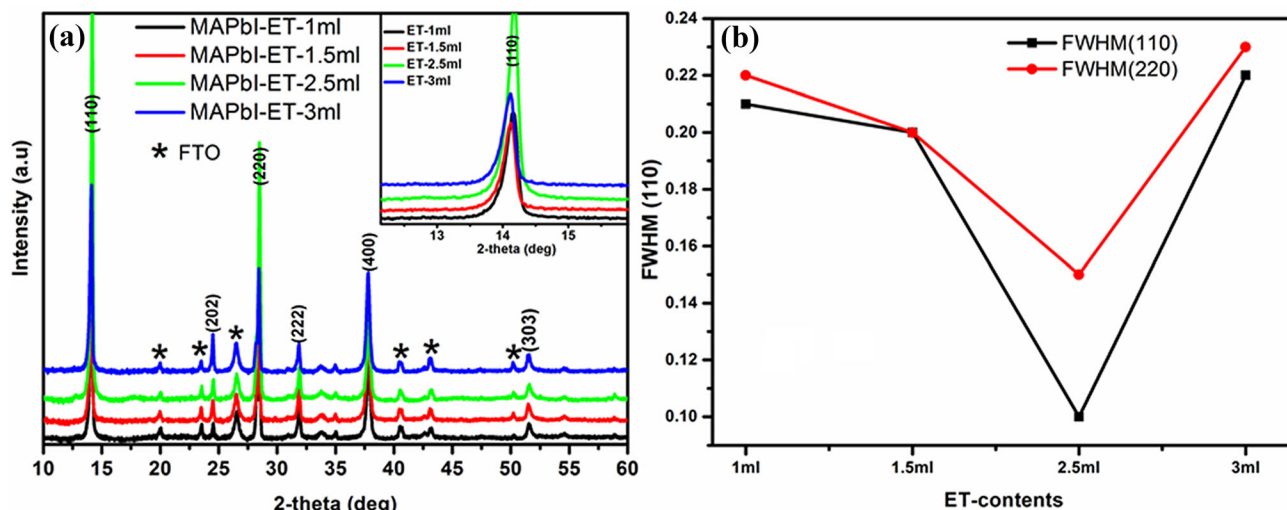


Fig. 1. (a) The obtained XRD patterns with different amounts of antisolvent, (b) the full width at half maximum (FWHM) for the (110) and (220) peaks.

ray diffraction (XRD), transmission electron microscope (TEM), atomic force microscopy (AFM) and UV-visible spectrometer.

EXPERIMENTAL PROCEDURE

Film Preparation

The perovskite absorber lead halide hybrid MAPbI₃ was elaborated using different commercially available precursors. In particular, the compounds lead iodide (PbI₂), methylammonium iodide (MAI) were used, and dimethyl sulfoxide (DMSO) and N, N-dimethylformamide (DMF) as solvents. The prepared solution of MAPbI₃ was spin-coated onto a fluorine-doped tin oxide substrate at 5000 rpm for 30 s. Before the surface changed to turbid, caused by rapid vaporization of DMF, ET was rapidly dripped (not dropwise) onto the rotating substrate producing optimum morphology and good crystallinity. On the other hand, samples which were dripped slowly by ET with a delay of time (like dropwise) show poor morphology and crystallinity.

The transparent films were subsequently annealed at low temperature (slow thermal annealing), 60°C for 5 min, which converted to a dark brown film upon heating. In the rapid thermal annealing process, the prepared films were annealed at high temperature 100°C for 10 min, as shown in Fig. 3.

Film Characterization

The structural properties were characterized by x-ray diffraction with a RIGAKU Ultima IV diffractometer within the 2θ range of 10° to 60° at room temperature using CuK α radiation ($\lambda = 1.5418$ Å). The surface morphology of the films was analyzed by SEM (Quanta 200—FEI) with measurement conditions of 1.5 kV at various magnifications. AFM measurements were made by using a Nano Surf Mobile S instrument in tapping mode, with a

voltage scan applied to the cell from -1.5 V to $+1.5$ V at a scan rate of 0.5 Hz. TEM (JEO-JEM-1010) measurement conditions were 2.5 kV at various magnifications. Absorption measurements were performed using an Ocean Optics HR4000 spectrophotometer (Si-CCD) between 300 nm and 850 nm wavelengths. Photoluminescence (PL) measurements were made with a He-Cd laser source emitting at 325 nm, and a back-thinned Si-CCD detector (Hamamatsu) detected the PL emissions.

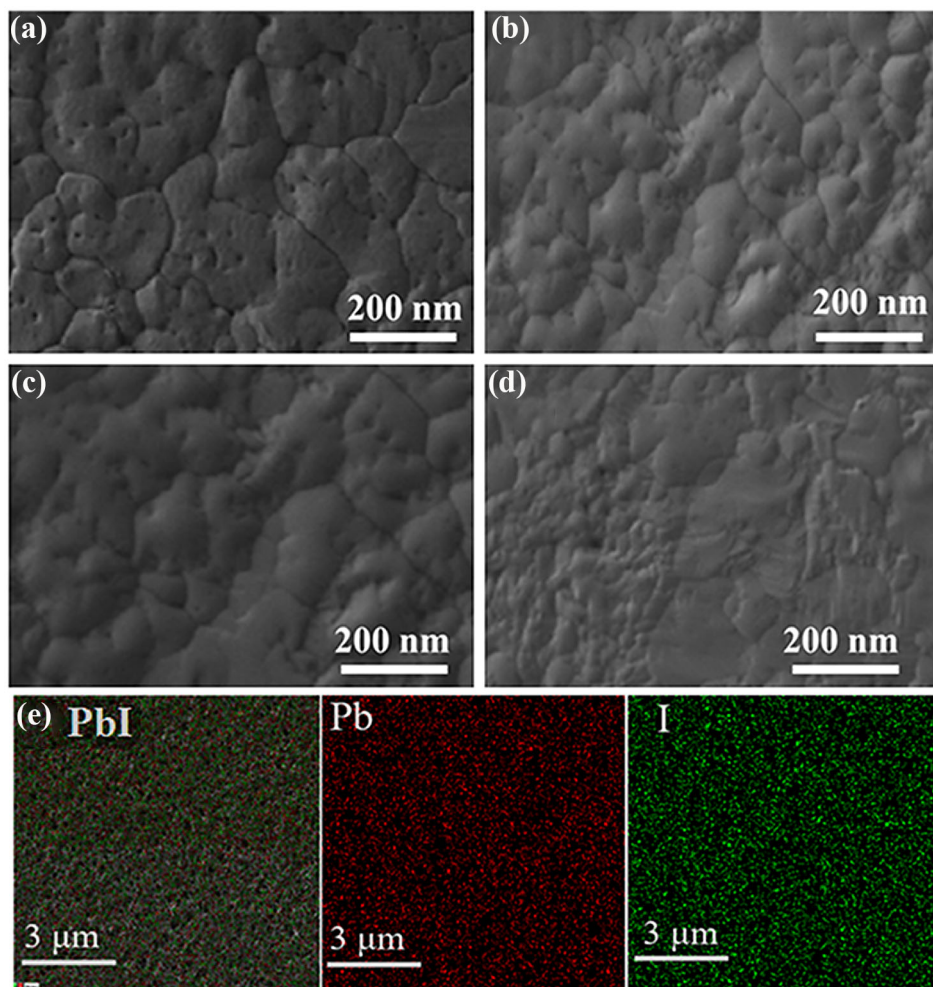
RESULTS AND DISCUSSION

The impact of the antisolvent treatment on the microstructure of the thin films was examined by XRD as shown in Fig. 1a, from which it can be seen that several diffractions peaks are located at 14.0, 24.0, 28.0, 32.0, 37.5, and 52.0, which correspond to the planes of (110), (202), (220), (222), (400), and (303) respectively. The same diffraction peaks are correlated with the previous MAPbI₃ structure study.^{9,10} In addition, it was found that the intensity of the (110) peak is increased when the added volume of the ET varies from 1 ml to 2.5 ml. However, when the ET quantity is greater than the optimal value of 2.5 mL, the (110) peak intensity decreases due to the high solubility of MAI, which causes its removal from the perovskite structure. The XRD pattern revealed the improved crystallite orientation along the (110) plane. Such preferential orientation can originate from the pre-crystallization step of the MAPbI₃ crystallites in the presence of the solvent treatment. All perovskite films crystallize in a tetragonal lattice corresponding to the space group I4/mcm. The lattice parameters were found to be $a = b = 8.919$ Å, and $c = 11.920$ Å.

Figure 1b shows that the peaks (110) and (220) the full width at half maximum (FWHM) values decrease for the samples treated with 3 ml of ET for different peak characteristics of MAPbI₃. Effective

Table I. The grain size, dislocation density and lattice strain of XRD of MAPbI₃ thin films

Sample ID	Grain size (nm)	Roughness (nm)	Dislocation density (nm ⁻¹)	Lattice strain (ϵ)
ET-1 ml	310	39	1.04×10^{-05}	0.38
ET-1.5 ml	333	41	0.90×10^{-05}	0.39
ET-2.5 ml	400	46.73	0.62×10^{-05}	0.39
ET-3 ml	300	36.99	1.11×10^{-05}	0.37

Fig. 2. SEM images of MAPbI₃ with different amounts of antisolvent ET: (a) 1 ml, (b) 1.5 ml, (c) 2.5 ml, (d) 3 ml and (e) mapping of halide perovskite.

lattice strain has been calculated to have an idea about the deficiencies and deformations of the grains in the thin film. Equation 1 was used to determine the effective lattice strain (ϵ). The grain size (D) of the films has been found in the range of 310 nm to 400 nm (Table I).

$$\beta \cos(\theta) = \frac{k\lambda}{D} + 4\epsilon \sin(\theta) \quad (1)$$

where θ is the Bragg angle, K is a constant (0.94), β is the FWHM, and λ is the wavelength of the x-ray. The dislocation density of the crystal was evaluated using Eq. 2.

$$\delta = \frac{1}{D^2} \quad (2)$$

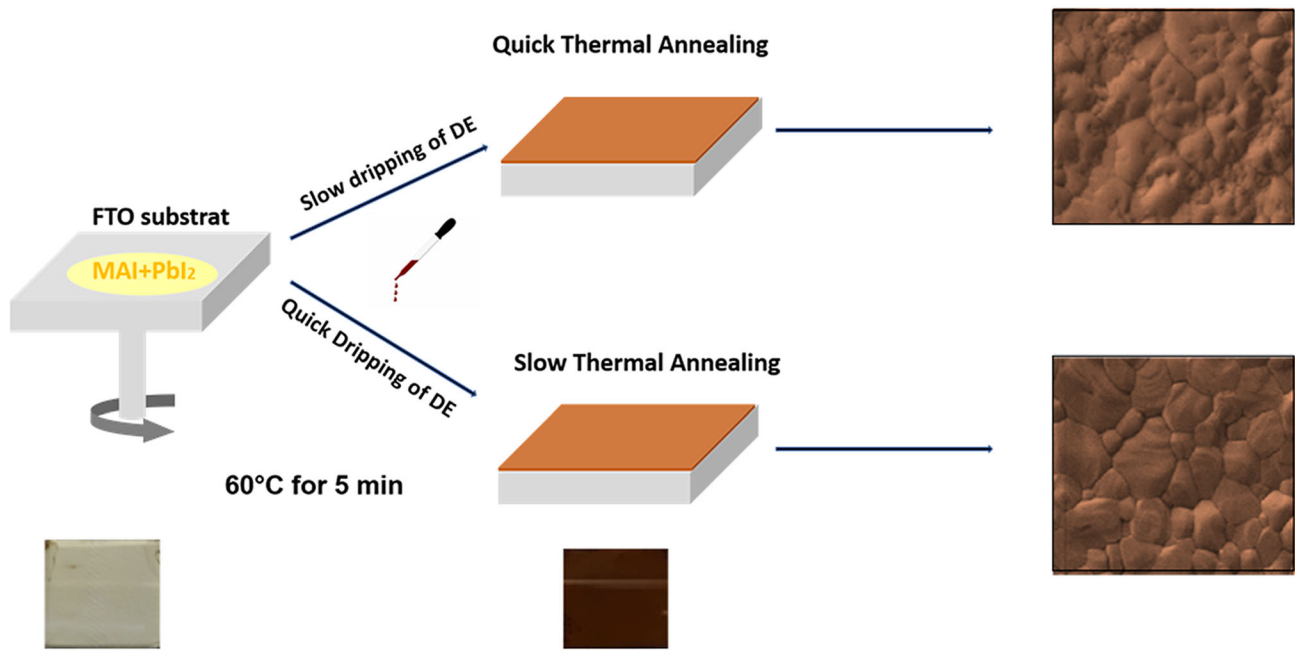


Fig. 3. A schematic representation of two-step antisolvent additions.

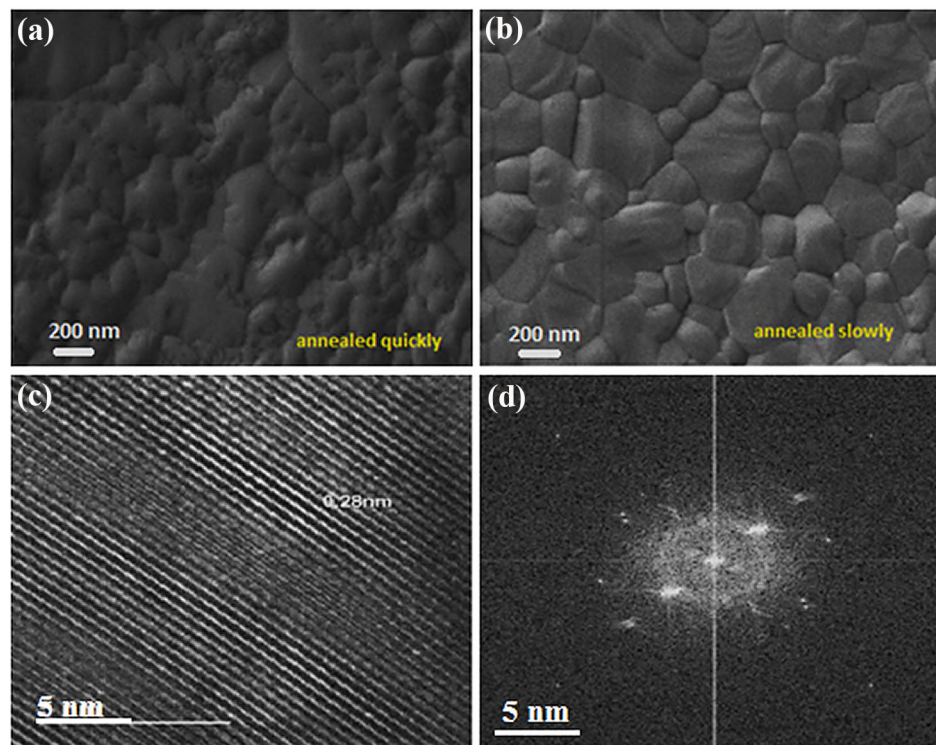


Fig. 4. SEM images of (a) rapid and (b) slow thermal annealing for 60 min and 100 min, respectively, (c) HRTEM images and (d) electron diffraction spectrum of the interface.

As summarized in Table I, for the grain size, dislocation density, and lattice strain values, it was found that the grain size significantly increases upon the addition of ET 1 ml, 1.5 ml, 2 ml, and 2.5 ml, 310 nm, 333 nm and 400 nm, respectively, whereas the grain size decreased by 300 nm upon

the addition of ET 3 ml. This indicates that the addition of more than the optimum level (2.5 ml) affects the grain sizes and other related parameters, which is good agreement with the XRD analysis. The XRD study revealed the good impact of ET antisolvent treatment on the samples.

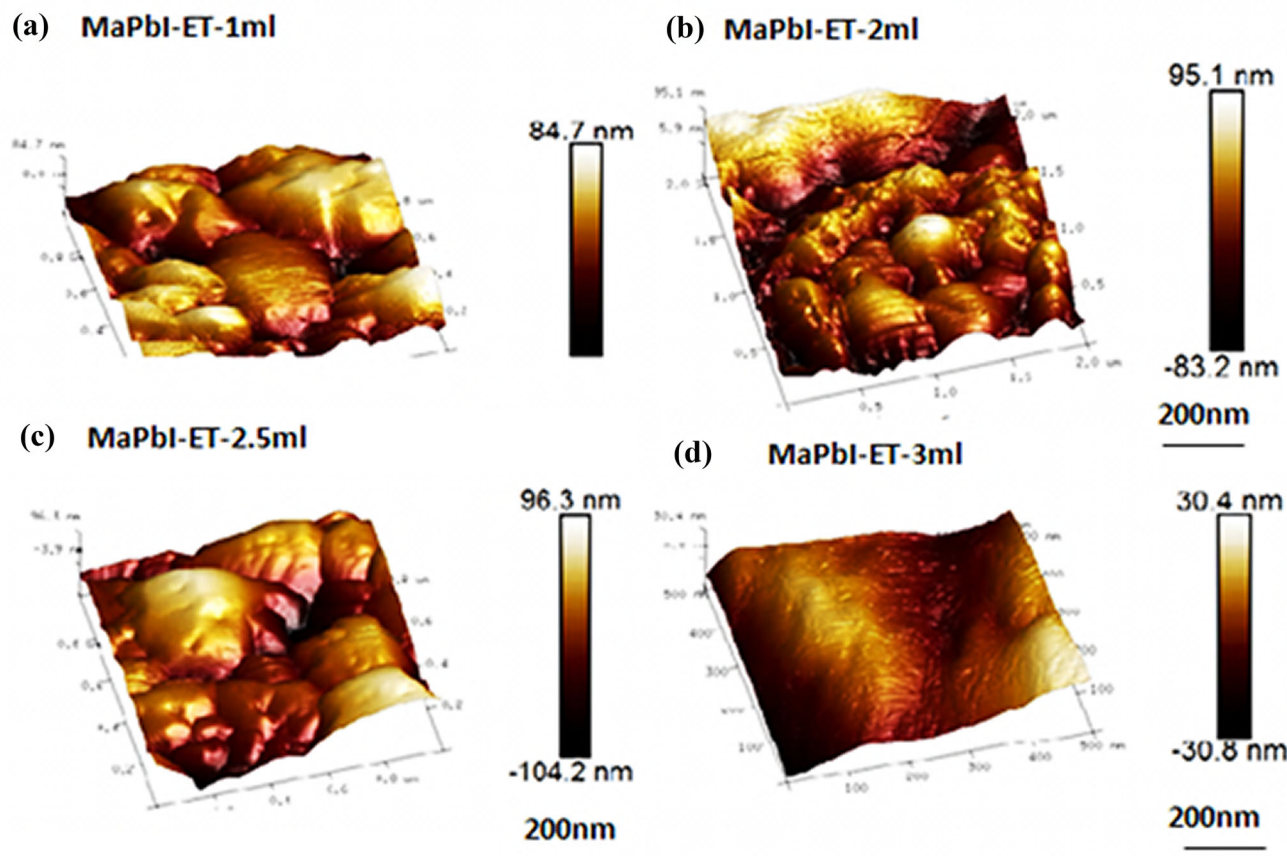


Fig. 5. AFM images of perovskite multiple-cation halide perovskite films, MAPbI_3 , upon the addition of different amounts of antisolvent ET.

Figure 2 displays the SEM images of multiple-cation halide perovskite films, MAPbI_3 , upon the addition of different amounts of the antisolvent ET. It can be observed that the surface morphology contained the irregular size of the grain boundaries of the thin films.

Figure 2a, b, c, and d shows SEM images of the results of the addition of 1 ml, 2 ml, 2.5 ml, and 3 ml ET, respectively. Furthermore, the addition of ET 3 ml makes the film surface flatter with the reduction of the size of the grain boundary. Additionally, for the surface morphology improvement, the sample of 2.5 ml ET was thermally annealed with two different processes, rapidly and slowly.^{11,12}

It can be perceived from the process shown in the schematic diagram in Fig. 3 that the rapid addition of antisolvent can enhance the homogeneity of the surface and form small crystals Fig. 4a. On the other hand, the slow addition of antisolvent reduces the solubility of the solute and consequently generates supersaturation^{13,14} to accelerate the crystallization process (Fig. 4b). Moreover, thermal annealing plays an important role on the surface and the crystallography of the films. In Fig. 4a, annealed at 60°C for 5 min, and (b), the temperature is gradually increased at 100°C for 10 min, it can be seen that the crystal and grain sizes are significantly increased with the increasing annealing temperature.

Figure 4c shows a TEM analysis of MAPbI_3 thin-film monocrystal with lattice fringe spacing of 0.28 nm corresponding to (110) or (220) of the tetragonal MAPbI_3 phase. This result has already been confirmed by the XRD pattern (Fig. 1a), where Fig. 4c shows the selected area of the electron diffraction spectrum revealing that the MAPbI_3 thin films are polycrystalline.¹⁵

Figure 5 represents the AFM analysis of the MAPbI_3 area of $2\ \mu\text{m} \times 2\ \mu\text{m}$ treated by different ET additives (1 ml, 1.5 ml, 2.5 ml, and 3 ml). The surface morphology and roughness vary, which is calculated by the root-mean-square (R_{rms}) showing dramatic changes of 39 nm, 41 nm, and 46.73 nm for ET 1 ml, 1.5 ml, and 2.5 ml, respectively. The results are summarized in Table I. On the other hand, the R_{rms} decreases to 36.99 nm by the addition of 3 ml ET (Fig. 5d), although the use of 2.5 ml of ET shows strong absorption from the visible to near infrared region. The large size of the hills and troughs makes the surface rougher in the AFM analysis. The morphology is correlated to the amount of ET until a certain point at which the surface roughness started to decrease in size.

The PL measurements were recorded at ambient temperature shown in Fig. 6a. It can be seen that the PL peak intensity in the range of 700–850 nm reported before¹⁶ gradually increases with an increasing

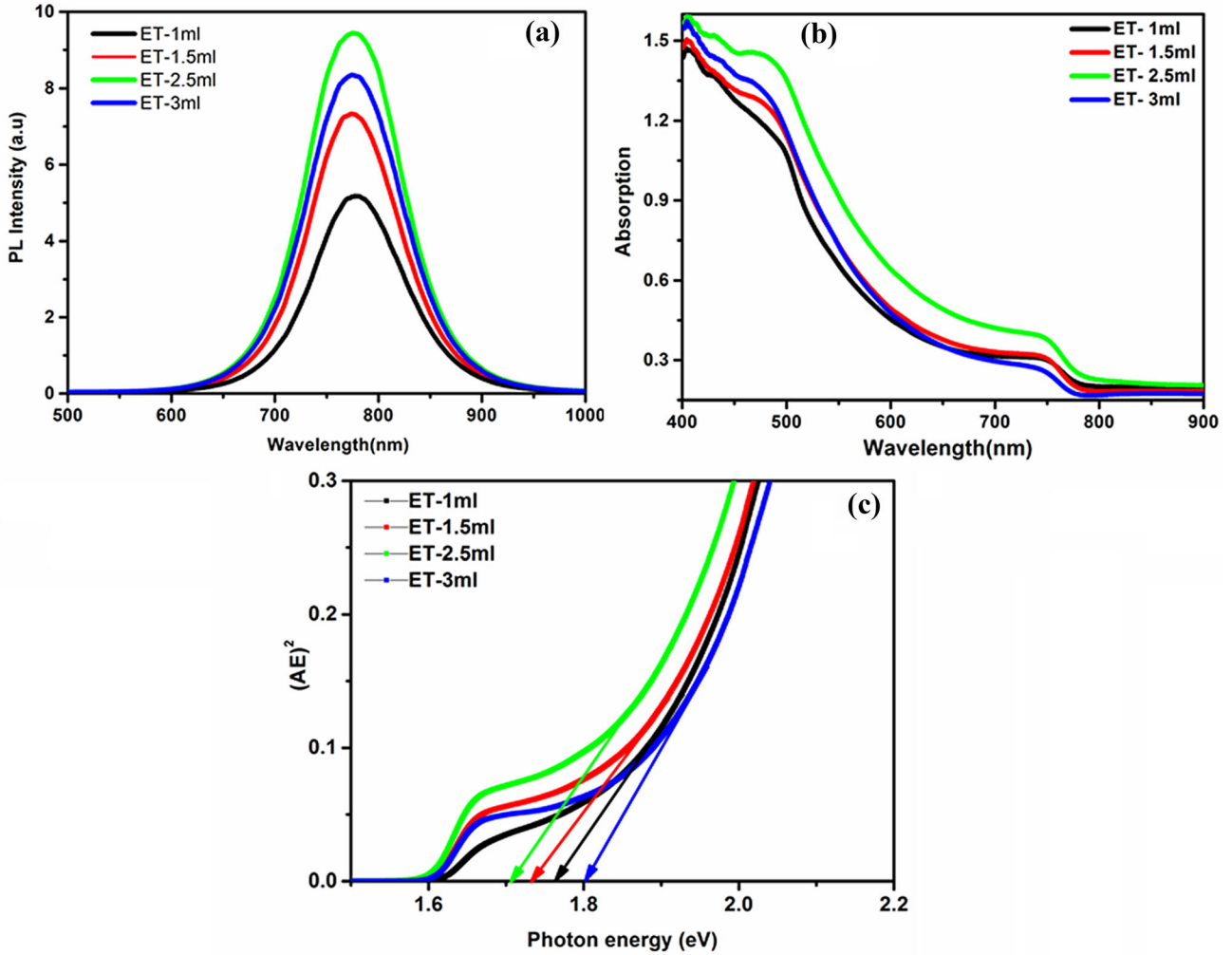


Fig. 6. (a) PL perovskite thin films of MAPbI₃ upon addition of different amounts of antisolvent ET, (b) UV-Vis absorption, and (c) optical bandgap of MAPbI₃.

Table II. Band gap of the MAPbI₃ thin films with different amounts of antisolvent ET

Sample ID	PL		Absorption		Stokes shift (meV)
	λ (nm)	E _g (eV)	λ (nm)	E _g (eV)	
ET-1 ml	779	1.59	700	1.77	180
ET-1.5 ml	784	1.58	720	1.72	140
ET-2.5 ml	789	1.57	729	1.70	130
ET-3 ml	784	1.58	788	1.80	220

amount of ET. However, by adding more than 2.5 ml of ET, the PL intensities begin an inverse change. A suggestion that ET 2.5 ml is the optimal level for where it can trap more light. This result also supports the morphology and the crystal quality improvement of perovskite thin films. The corresponding UV-Vis spectra of MAPbI₃ were recorded between 400 nm and 900 nm (Fig. 6b). It can be observed that different ET concentrations shift the absorption edge to the high wavelength. The most obvious is the absorption shift

due to the improvement of the crystallinity and surface passivation, which reduces the defect density of the MAPbI₃ films and increases their crystallization quality. Furthermore, the optical bandgap is in good agreement where the bandgap dramatically decreases until an optimal level (Fig. 6c). The ET antisolvent regulates the optical properties of MAPbI₃ semiconductor materials for photovoltaic devices.¹⁷⁻¹⁹ The optical bandgap and corresponding wavelength are summarized in Table II.^{20,21}

DEGRADATION STUDY

The two main environmental factors that affect photovoltaic stability are oxygen and humidity. Here, we studied the degradation mechanism of MAPbI₃ films deposited using the ET antisolvent treatment. Perovskite films were kept under dark conditions at 60%. To evaluate the degradation of the MA samples, we examined the structural and morphological changes of the 2.5 ET-MAPbI₃ sample after 4 weeks. The degradation of the MAPbI₃ is most probably initiated by the H₂O molecules present in the air, leading to the slow fall of the MAPbI₃ lattice and therefore a change of the film color from dark black to brownish, as shown in supplementary Fig. S1.

Further, we examined the surface of the layer by SEM (see supplementary Fig. S2 (a, b)). The morphology of the perovskite layer, MAPbI-ET-2.5 ml, showed a granular and rather inhomogeneous topography and grain boundaries which are ideal for the study of the degradation process. In supplementary Fig S2(c), the XRD spectrum after 4 weeks is dominated by the strong PbI₂ peak, indicating the decomposition of the MAPbI₃ structure to PbI₂. The degraded yellow areas continued to grow until taking over all the film area after 4 weeks. Our results can explain the rate of degradation and the origin of the enhanced performance and stability.^{22–24}

CONCLUSION

We have efficiently presented the use of antisolvent ET with a precise amount to improve the performance of MAPbI₃ perovskite solar cells. The characterization by XRD shows a high intensity by the treatment, and SEM images also reveal that the addition of ET greatly affects the crystalline process of MAPbI₃ and causes an increase in the grain size of the perovskite thin film. The increase of the grain size may result from an increase in the light absorption of the perovskite layer if the use of ET is optimized, In our study, optimizing the addition of ET in perovskite-based solar cells based on MAPbI₃ can increase the yield well.

ACKNOWLEDGEMENT

This work was supported by Ministerio de Economía y Competitividad (Grant Number ENE2016-77798-C4-2-R).

CONFLICT OF INTEREST

The authors declare that they have no conflict of interest.

ELECTRONIC SUPPLEMENTARY MATERIAL

The online version of this article (<https://doi.org/10.1007/s11837-020-04518-5>) contains supplementary material, which is available to authorized users.

REFERENCES

1. A. Bouich, S. Ullah, B. Marí, L. Atourki, and M.E. Touhami, *Mater. Chem. Phys.* 258, 123973 (2021).
2. A. Bouich, S. Ullah, H. Ullah, M. Mollar, B. Marí, and M.E. Touhami, *JOM* 72(2), 615 (2020).
3. C. Quarti, E. Mosconi, J.M. Ball, V. D'Innocenzo, C. Tao, S. Pathak, and F.D. Angelis, *Energy Environ. Sci.* 9, 155 (2016).
4. J.H. Im, H.S. Kim, and N.G. Park, *Appl. Mater.* 2, 081510 (2014).
5. M.J. Carnie, C. Charbonneau, M.L. Davies, J. Troughton, T.M. Watson, K. Wojciechowski, and D.A. Worsley, *Chem. Commun.* 49, 7893 (2013).
6. D. Bi, S.J. Moon, L. Häggman, G. Boschloo, L. Yang, E.M. Johansson, and A. Hagfeldt, *RSC Adv.* 3, 18762 (2013).
7. Q. Chen, H. Zhou, Z. Hong, S. Luo, H.S. Duan, H.H. Wang, and Y. Yang, *J. Am. Chem. Soc.* 136, 622 (2013).
8. M.R. Leyden, L.K. Ono, S.R. Raga, Y. Kato, S. Wang, and Y. Qi, *J. Mater. Chem. A* 2, 18742 (2014).
9. W. Kong, Z. Ye, Z. Qi, B. Zhang, M. Wang, I.A. Rahimi, and H. Wu, *Phys. Chem. Chem. Phys.* 17, 16405 (2015).
10. X. Guo, C.M. Cleese, C. Kolodziej, A.C. Samia, Y. Zhao, and C. Burda, *Dalton Trans.* 45, 3806 (2016).
11. Z. Xiao, Q. Dong, C. Bi, Y. Shao, Y. Yuan, and J. Huang, *Adv. Mater.* 26, 6503 (2014).
12. S. Luo and W.A. Daoud, *Materials* 9, 123 (2016).
13. N.G. Park, *CrystEngComm* 18, 5977 (2016).
14. X. Zheng, B. Chen, C. Wu, and S. Priya, *Nano Energy* 17, 269 (2015).
15. Q. Jeangros, M. Duchamp, J. Werner, M. Kruth, R.E. Dunin-Borkowski, B. Niesen, and W.A. Hessler, *Nano Lett.* 16, 7013 (2016).
16. D. Liu, J. Yang, and T.L. Kelly, *J. Am. Chem. Soc.* 136, 17116 (2014).
17. H. Zhang, M. Lyu, Q. Wang, J.H. Yun, and L. Wang, *Chem. Commun.* 50, 11727 (2014).
18. J.J. Choi, X. Yang, Z.M. Norman, S.J. Billinge, and J.S. Owen, *Nano Lett.* 14, 127 (2013).
19. A. Halder, R. Chulliyil, A.S. Subbiah, T. Khan, S. Chattoraj, A. Chowdhury, and S.K. Sarkar, *J. Phys. Chem. Lett.* 6, 3483 (2015).
20. S. Ullah, A. Bouich, H. Ullah, B. Marí, and M. Mollar, *Sol. Energy* 208, 637 (2020).
21. A. Bouich, S. Ullah, H. Ullah, B. Marí, B. Hartiti, M.E. Touhami, and D.M.F. Santos, *J. Mater. Sci.: Mater.* 30(23), 20832 (2019).
22. G. Abdelmageed, L. Jewell, K. Hellier, L. Seymour, B. Luo, F. Bridges, and S. Carter, *Phys. Lett.* 109, 233905 (2016).
23. J. Li, Q. Dong, N. Li, and L. Wang, *Adv. Energy Mater.* 7, 1602922 (2017).
24. N. Aristidou, M.I. Sanchez, T. Chotchuangchutchaval, M. Brown, L. Martinez, T. Rath, and S.A. Haque, *Angew. Chem. Int. Ed.* 54, 8208 (2015).

Publisher's Note Springer Nature remains neutral with regard to jurisdictional claims in published maps and institutional affiliations.